Supplementary Information for "Persistence of Strong Silica-Enriched Domains in the Earth's Lower Mantle"

Maxim D. Ballmer[1,2], Christine Houser[1], John W. Hernlund[1], Renata M. Wentzcovitch[1,3,4] & Kei Hirose[1]

[1]*Earth-Life Science Institute, Tokyo Institute of Technology, Meguro, Tokyo, Japan.*
[2]*Institute of Geophysics, ETH Zurich, Zurich, Switzerland.*
[3]*Department of Applied Physics and Applied Mathematics, Columbia University, New York, USA.*
[4]*Department of Earth and Environmental Sciences, Columbia University, Lamont-Doherty Earth Observatory, Palisades NY, USA.*

1 Influence of composition on viscosity and buoyancy

In this study, we considered the influence of Mg/Si variations on viscosity and density, two key parameters governing mantle flow. The lower mantle is thought to be dominantly composed of the rheologically strong (Mg,Fe)SiO_3-bridgmanite (Br) phase and the relatively weak (Mg,Fe)O-ferropericlase (Fp) phase. The simplest model for deformation of a rock containing two phases is the "load bearing framework" (LBF), which is valid when strain is equally partitioned between weak grains and strong grains. The LBF approximation yields a simple linear dependence of rock viscosity upon volume fraction of one of the phases[1]. However, in rocks containing a mixture of rheologically weak and strong phases, stain is thought to be inequally partitioned. Such aggregates can hence exhibit much more dramatic variations in deformation strength and style than predicted by the LBF model, particularly if the ratio of viscosity between the two phases exceeds one order of magnitude. For large viscosity contrasts, the weak phase may become stretched and smeared between strong grains upon deformation, and if it is abundant enough to form an inter-connected network, the weaker phase may dominate the rheology of the aggregate even at modest volume fractions. As Fp is much weaker than Br, the non-linear "inter-connected weak layers" (IWL) model[1] is more appropriate, and is often invoked in viscosity estimates of lower-mantle rocks[2–4] (Suppl. Figure S5).

In the IWL model, the largest variations in viscosity occur for modal abundances of the weak phase between 0% and $\sim$30%. At model abundances of $\sim$30% and beyond, only minor variations occur, because rock viscosity is ever dominated by that of the weak phase in this range[1] (Suppl. Figure S5). The full variation in viscosity thus occurs over a range that is similar to realistic

variations in Fp content in the Earth's lower mantle, based on present uncertainties in terms of the Mg/Si ratio. Therefore, the total viscosity contrast between putative SiO_2-enriched domains in the lower mantle and pyrolitic materials could be almost as large as the viscosity contrast between the strong and weak phases, i.e., up to three orders of magnitude.

Nevertheless, many uncertainties persist, for example in terms of the exact viscosity contrast between Br and Fp, dominant deformation mechanisms[3–5], as well as the amplitude of Mg/Si variations in the lower mantle. Additionally, the IWL model itself may be too simplistic to capture the full complexity of deformation behavior at high pressures and temperatures over geological time scales. Rock deformation is influenced by strain history, fabric, grain growth and dynamic recrystallization. Also, the viscosity contrast between Fp and Br is thought to vary as a function of depth[3,6]. In the light of these uncertainties, we explored the effects of the viscosity contrast between SiO_2-enriched rock and pyrolitic rocks, a free parameter in our geodynamic models. We find that modest and well-realistic viscosity contrasts of $\sim 30\times$ are sufficient for a shift in the regime of mixing of the Earth's mantle to stabilize BEAMS over the age of the Earth (see Figure 2 in the main text).

The densities of Fp and Br are similar, but not identical, due to differences in crystallographic structure. Br is slightly denser than Fp. Thus, a variation in Mg/Si also leads to a slight variation in density of the whole rock in the lower mantle. According to the calculations described in the method section, the density difference between Br and Fp steadily decreases from around 1.8% at the top of the lower mantle to around 0.8% at the base of the mantle for the same Fe/(Mg+Fe). The decrease in density contrast from 1.8% to 0.8% with increasing pressure is due to differences in bulk moduli between Br and Fp. Thus a variation of $\sim$20% in Fp modal abundance, such as between pyrolite and perovskitite, naturally gives rise to a contrast of 0.16$\sim$0.36% in total rock density. This change in density (i.e., before any additional changes due to variations in Fe/(Mg+Fe)) overlaps with the ideal range of density contrasts for BEAMS persistence of 0.2$\sim$1.2% as are predicted by our geodynamic models (see Figure 2 in the main text).

2 Analysis of numerical-model predictions

In our suite of geodynamic models with variable density and viscosity contrasts, we observe two different regimes of mantle convection: (A) efficient mantle mixing and (B) long-term preservation of BEAMS (see main text). For details of the numerical approach, see method section. In order to distinguish between the two regimes, we analyzed the distribution of materials after 4.6 Gyrs in the model domain. Each finite element contains a mixture of materials (or material tracers),

with compositional index ranging from zero to one (0: SiO_2-poor; 0.9-1.0: SiO_2-rich materials). Histograms of compositional distributions after 4.6 Gyrs model time (Suppl. Figure S6) reveal that only a subset of models display bimodal compositional distributions with significant preservation of SiO_2-rich material. These are the cases in which BEAMS are manifested. All other cases display unimodal distributions with one peak near compositional index 0.5.

In order to quantitatively discriminate between regimes, we evaluated the fraction of primordial SiO_2-rich material that has been preserved over 4.6 Gyrs of mantle convection and mixing (see Figure 2 in the main text). This preservation fraction is calculated as the number of finite elements (i.e., anywhere in the model box) with compositional index $\geq$0.84 divided by the number of elements of the lower mantle. For example, it would be 100% if the lower mantle was entirely made up of SiO_2-enriched materials with compositional index $\geq$0.84, and the upper mantle entirely of material with compositional index $<$0.84, as is the case for the initial condition.

We defined the boundary between regimes A and B at preservation fractions of $\sim$15%, consistent with visual analysis of model results. In any case, fractions of primordial SiO_2-enriched material preserved after 4.6 Gyrs usually range far below 15% for regime A, and between 20% and 40% for regime B (see Suppl. Table 3). Accordingly BEAMS are predicted to make up 20%–40% of the lower mantle, or about 13%–26% of the entire mantle at the present day. Note however that these values would be lower in the 3D spherical-shell Earth's mantle, simply due to geometry. The lower mantle makes up a smaller fraction of the whole mantle in spherical geometry than in the modelled Cartesian geometry (also see below).

Figure 2 in the main text shows the boundary between regimes A (efficient mixing) and B (preservation of BEAMS) within the parameter space of variable $\Delta\rho$ and Φ. One complication involves that each of the model cases displays a somewhat distinct effective-viscosity profile (through time), mostly as a function of Φ. As the relevant viscosity profile controls convective vigor, and hence strongly affects mixing efficiency, the exact relevant location of the regime boundary within the parameter space remains somewhat uncertain. We quantify convective vigors by reporting the characteristic convective heat flux, or Nusselt number *Nu*, at $\sim$4.6 Gyr (i.e., as an average over model times 4.1–5.1 Gyrs). Note that *Nu* strictly measures the non-dimensional convective heat flux, but should be directly related to convective vigor[7], at least at given thermal-boundary-layer thicknesses, which remain virtually constant across all cases modeled (see Suppl. Table S3).

To avoid comparing cases with strongly variable *Nu*, we performed three additional cases with low Φ (see circles in Figure 2 of the main text). In these "reference" cases, an additional viscosity jump at 660 km depth of $\lambda > 0$ is imposed in order to obtain effective-viscosity profiles and

convective vigors similar to those of higher-Φ models. This similarity is confirmed by comparing *Nu* between cases. For example, in Figure 2 of the main text, cases with similar *Nu* (i.e., in the range of 10–11) are highlighted yellow. Any boundary between regimes A and B based on these cases alone is similar to the boundary shown (grey line; based on all cases). This similarity confirms that our main conclusions in terms of numerical-model analysis (see below and main text) are robust.

Finally, individual analysis of reference cases shows that a viscosity jump in the mid-mantle alone is insufficient to promote large-scale preservation of distinct lower mantle domains. For example, reference case I with $\lambda = 8$ but without any effects of composition on density or viscosity (i.e., $\Phi = 1$ and $\Delta\rho = 0$ kg/m^3) displays efficient mantle mixing and a unimodal distribution of composition for *Nu*=10.2. Reference cases II and III confirm that small Φ=6 and/or moderate $\Delta\rho$=35 kg/m^3 are also insufficient to avoid efficient mixing at *Nu* of $\sim$10.5 (see Suppl. Table 3). Note that the λ imposed in the reference cases are chosen to tune Nusselt number to $10 \leq Nu \leq 11$. Thereby, the λ imposed in the reference cases remain lower bounds[8,9], mostly because we took the simplfied assumption of $\lambda = 1$ in all other cases. The latter choice implies that viscosities in the upper mantle are upper bounds, taken to limit computational costs.

We stress that all our cases with $10 \leq Nu \leq 11$ have similar and overall realistic properties of convection, at least in the lower mantle. Maximum lower-mantle velocities in these cases (highlighted in Figure 2 of the main text) are on the order of $\sim$2 cm/yr, consistent with inferred slab-sinking speeds[10]. Lower-mantle viscosities are also in the realistic range[8] (see Figure 1e in the main text). Finally, dimensionalizing the above-mentioned Nu yields core-cooling-related heat fluxes of $\sim$30 mW/m^2, which are similar to those observed ($\sim$65 mW/m^2) as long as radioactive heating accounts for another $\sim$35 mW/m^2 on Earth.

We conclude that compositional-viscosity contrasts of $\Phi > 20$ are essential for large-scale preservation of BEAMS (see Figure 2 of the main text). The preservation of BEAMS is an attractive scenario to address the survival of primordial geochemical reservoirs in the mantle[11,12]. An alternative scenario involves that primordial material may be preserved as piles at the base of the mantle due to the effects of intrinsic density contrasts $\Delta\rho$ of $\sim$3% alone[13–15]. Intrinsically-dense piles, or large low shear-velocity provinces (LLSVP)[16,17], and intrinsically-strong BEAMS may indeed be manifested together in the present-day lower mantle (see Figure 4 of the main text).

3 Manifestation of BEAMS in the present-day Earth's mantle

This study explores the formation of BEAMS in a 2D-Cartesian geometry, which is the simplest and most computationally efficient way to explore the essential elements of the dynamics within an extensive parameter space. The organization of convection in the BEAMS regime involves encapsulation of high-viscosity material in the core of convection cells, with low-viscosity material circulating around high-viscosity material within conduits. Such an arrangement minimizes viscous dissipation because it focuses deformation in low-viscosity materials through kinematic strain localization, and minimizes deformation in high-viscosity materials[18]. We suggest that BEAMS in the 3D spherical-shell mantle would likewise assume planforms that minimize internal deformation of high-viscosity materials. Accordingly, we expect these planforms to involve roll segments, or toroid-shaped geometries. By "segments" we refer to rolls of finite axial extent, while toroids would be donut-shaped features.

The details of BEAMS shapes hinge on whether BEAMS actually rotate or mostly remain stationary. The actual extent of BEAMS rotation should depend on the rheological coupling between BEAMS and the pyrolitic mantle that circulates around BEAMS. For non-linear rheology[4], coupling and hence BEAMS rotation is expected to be weaker than predicted by the models. Also note that inside-out rotation of donut-shaped BEAMS in the 3D spherical mantle may be strongly inhibited.

It is also important to note that the fraction of mantle occupied by BEAMS is exaggerated in our 2D models, and will be smaller in the 3D-spherical Earth due to geometrical considerations. For example, the relative lower-mantle volume alone is smaller in 3D-spherical than in 2D-Cartesion geometry. If we consider BEAMS extending from 900$\sim$2,300 km depth as roughly roll-shaped structures (in this example $\sim$1,500 km in diameter), then a single 10,000 km long roll spanning $\sim$120 degrees of arc through the lower mantle would occupy $\sim$2% of the mantle's volume. Guided by our preliminary map (see Figure 3 in the main text, and discussion below), BEAMS might plausibly be assembled from 40,000-60,000 km total length of roll-like structures, hence occupying 8%$\sim$12% volume of the mantle. The mass fraction of these BEAMS will be slightly higher owing to the elevated density of the lower mantle, giving roughly 10%$\sim$15% of the mantle.

The current geometrical manifestation of BEAMS in the present-day lower mantle is not obvious from seismic-tomography models. The difficulty of imaging BEAMS (if they exist) is related to the small expected seismic contrasts between BEAMS and downwelling slabs (Suppl. Figure S7; also see below). Figure 3 in the main text shows an attempt to map BEAMS as well as

upwelling/downwelling conduits. This attempt is guided by radially-averaged seismic shear velocity variations in the depth range of 1,000-2,200 km depth. This depth range should represent radial structure of the mid mantle by minimizing effects of the transition zone and the LLSVPs[19,20]. If we assume that conduits between the BEAMS are radially coherent features, then depth-averaging should amplify these features. As an additional guide, the location of stagnant slabs are labeled ("S")[21,22], considering that slabs may stagnate because they encounter high-viscosity BEAMS (see main text). Indeed, slab stagnation generally occurs somewhere between lower-mantle downwelling conduits (i.e., deep-sinking Tethys and Farallon slabs) and upwelling centers (i.e., beneath the south-central Pacific and Africa). In any case, note that either of the above criteria may be imperfect for mapping BEAMS, since conduits could be irregular or tilted, and alternative mechanisms may lead to slab stagnation, in addition to BEAMS[23,24]. Nevertheless, our estimate of BEAMS locations and geometry is consistent with cluster analysis of seismic-tomography models[25], given that the retrieved "neutral" cluster indeed contains BEAMS. Also note that first-order structural features in the mid-mantle such as low-velocity domains[20,25] (upwelling centers?) and high-velocity slabs of subducted Farallon and Tethys lithosphere[26] (downwelling conduits) are consistent across tomography models. Using this simple approach, we find that candidate upwelling and downwelling conduits assume the form of sheets or pillars, with intervening BEAMS assuming the form of finite rolls or donuts, compatible with the above dynamical arguments.

4 Comparing lower-mantle compositional models with PREM

In order to constrain lower-mantle composition, predictions for material properties of mantle rocks from experimental[27,28] and theoretical mineral physics[29–36] have been compared to 1D global seismic profiles (such as PREM[37]). However, such attempts have remained inconclusive, with proposed compositions ranging from perovskitite to pyrolite[38–46]. Much of this uncertainty in composition stems from an uncertainty in lower-mantle temperatures, given the trade-off between temperature and composition in terms of seismic velocities and density. For example, a 500 K shift in temperature changes the seismic velocity by about 1% in the lowermost mantle, similar to a shift in composition from pure Br to harzburgite. Therefore, a wide range of lower-mantle compositions may fit one-dimensional seismic profiles such as PREM within uncertainties for lower-mantle temperatures.

Supplementary Figure S2 demonstrates that both a homogenous-pyrolite-model and a BEAMS-model lower mantle (i.e., a mixture of 50% pure Br and 25% of each cold and warm harzburgite) yield a good fit to PREM, using a similar geotherm that is self-consistently calculated (see method section). The relevant geotherms are shown in Supplementary Figure S4. Thus, any comparisons

of mineral-physics predictions with PREM are insufficient to constrain the bulk composition of the lower mantle. Note that even a pure Br (i.e., perovskitite) lower mantle can produce an acceptable fit using lower-mantle temperatures that are shifted by +500 K (Suppl. Figure S8).

5 Slab "invisibility" in the lower mantle

One of the unresolved issues in the tomographic imaging of subducted oceanic lithosphere is the weak slab signal in the mid-mantle (see main text) bracketed by a strong slab signal in the transition zone and the top of the lower mantle, as well as near the core-mantle boundary[47]. We find that the enhancement of the ambient mid-mantle by SiO_2-enriched material (such as in the BEAMS hypothesis) can explain this observation since the velocity contrast between relatively cold harzburgite and temperate bridgmanite is less than between relatively cold harzburgite and temperate pyrolite (Suppl. Figure S7). Another effect involves the reduction of sensitivity of bulk modulus to temperature in the mid-mantle owing to the spin transition of iron in Fp[40], but note that this effect is already taken into account in computing the curves for this figure (see also method section). Thus, the weakening slabs signal in the mid-mantle can be better explained in the context of the BEAMS model than in that of the pyrolite model.

	SiO_2	MgO	FeO	CaO
pyrolite	48.01 (40.32)	40.89 (51.20)	7.67 (5.39)	3.43 (3.09)
harzburgite	44.16 (36.60)	46.17 (57.04)	8.76 (6.07)	0.91 (0.81)
bridgmanite	57.84 (50.15)	31.86 (41.18)	7.67 (5.51)	3.43 (3.19)

Supplementary Table 1: Compositions used in this study in wt.-% (mol-%). The original pyrolite composition is modified from ref. [48] by equally converting the 2.2 mol-% Al_2O_3 to MgO and SiO_2. The pure bridgmanite composition is derived by starting with the pyrolite composition and reducing the Mg/Si ratio until there is almost no free (Mg,Fe)O. The harzburgite is modified from ref. [34] by dividing the original 0.53 mol-% of Al_2O_3 equally between MgO and SiO_2.

Parameter	Symbol	Value
box height	z_{box}	2,900 km
box width	x_{box}	17,400 km
CMB temperature	T_{CMB}	3,000 °C
Rayleigh number	*Ra*	$2.68889 \cdot 10^7$
effective upper-mantle viscosity	ρ_m	$1.2 \cdot 10^{21}$ Pa·s
mantle reference density	ρ_m	4,500 kg/m^3
activation energy	*E**	35.662 kJ/mol
thermal diffusivity	κ	$2.5 \cdot 10^{-6}$ m^2/s
thermal expansivity	α	^{a}
viscosity contrast between materials	Φ	**1 – 249.1**
density contrast between materials	$\Delta\rho$	**0 – 65 kg/m^3**
viscosity jump at 660 km depth	λ	**1 – 8**
non-dimensional internal heating	***Q***	**0 – 1**

Supplementary Table 2: Parameters used in geodynamic models. The bottom four rows (bold) report the free parameters of the study (see Suppl. Table 3). (^{a}) For description of depth-dependent parameter α, see ref. [24]. *Ra* is calculated from ρ_m, which is valid for the upper mantle at potential temperatures of T_{CMB}.

Case	Φ	$\Delta\rho$ **(kg/m^3)**	λ	Q	**Nu**	**SiO_2-rich material preserved**
example	27.95	35	1	0	10.83	30.8%
reference I	1	0	8	0	10.2	2.18%
reference II	1	0	8	0	10.78	11.6%
reference III	6.0	0	2.5	0	10.56	3.9%
A0	3.14	0	1	0	11.61	0.41%
A10	3.14	10	1	0	12.58	0.13%
A20	3.14	20	1	0	11.72	0.02%
A35	3.14	35	1	0	11.71	0.01%
A50	3.14	50	1	0	12	0.01%
B0	8.91	0	1	0	11.81	3.79%
B10	8.91	10	1	0	11.45	5.05%
B20	8.91	20	1	0	11.71	6.71%
B35	8.91	35	1	0	11.72	6.46%
B50	8.91	50	1	0	11.15	1.03%
B65	8.91	65	1	0	11.19	0.35%
C0	27.95	0	1	0	10.45	8.86%
C10	27.95	10	1	0	10.83	13.23%
C20	27.95	20	1	0	10.83	30.75%
C35	27.95	35	1	0	10.84	30.8%
C50	27.95	50	1	0	10.7	18.81%
C65	27.95	65	1	0	10.34	12.09%
D0	79.43	0	1	0	9.45	9.05%
D10	79.43	10	1	0	10.24	31.85%
D20	79.43	20	1	0	10.49	37.34%
D35	79.43	35	1	0	10.22	36.76%
D50	79.43	50	1	0	9.55	20.63%
D65	79.43	65	1	0	9.44	0.01%
E0	249.07	0	1	0	9.33	33.25%
E10	249.07	10	1	0	9.4	37.09%
E65	249.07	65	1	0	8.05	49.39%

Supplementary Table 3: (previous page) List of all cases modeled. Controlling parameters (see Table S2) are given in columns 2–5. Key output variables in columns 6–7 (right side). Note that case C35 and the example case are the same case. The reported *Nu* is the average *Nu* over model times 4.1-5.1 Gyrs. The reported amounts of SiO_2-rich material preserved is calculated for model time 4.6 Gyrs (for details, see Suppl. Section 4).

6 Supplementary References

1. Takeda, Y. Flow in rocks modelled as multiphase continua: Application to polymineralic rocks. *Journal of Structual Geology* **20**, 1569–1578 (1998).

2. Yamazaki, D. & Karato, S.-I. Some mineral physics constraints on the rheology and geothermal structure of Earth's lower mantle. *Amer. Mineralogist* **86**, 385–391 (2001).

3. Marquardt, H. & Miyagi, L. Slab stagnation in the shallow lower mantle linked to an increase in mantle viscosity. *Nature Geoscience* **8**, 311–314 (2015).

4. Girard, J., Amulele, G., Farla, R., Mohiuddin, A. & Karato, S.-I. Shear deformation of bridgmanite and magnesiowüstite aggregates at lower mantle conditions. *Science* **351**, 144–147 (2016).

5. Kraych, A., Carrez, P. & Cordier, P. On dislocation glide in $MgSiO_3$ bridgmanite at high-pressure and high-temperature. *Earth and Planetary Science Letters* **452**, 60–68 (2016).

6. Piet, H. *et al.* Spin and valence dependence of iron partitioning in Earths deep mantle. *Proceedings of the National Academy of Sciences* **113**, 11127–11130 (2016).

7. Parmentier, E. M., Turcotte, D. L. & Torrance, K. E. Studies of finite amplitude non-Newtonian thermal convection with application to convection in the Earth's mantle. *Journal of Geophysical Research* **81**, 1839–1846 (1976).

8. Forte, A. & Mitrovica, J. Deep-mantle high-viscosity flow and thermochemical structure inferred from seismic and geodynamic data. *Nature* **410**, 1049–1056 (2001).

9. Rudolph, M., Lekic, V. & Lithgow-Bertelloni, C. Viscosity jump in Earth's mid-mantle. *Science* **350**, 1349–1352 (2015).

10. Van Der Meer, D. G., Spakman, W., Van Hinsbergen, D. J., Amaru, M. L. & Torsvik, T. H. Towards absolute plate motions constrained by lower-mantle slab remnants. *Nature Geoscience* **3**, 36–40 (2010).

11. Mukhopadhyay, S. Early differentiation and volatile accretion recorded in deep-mantle neon and xenon. *Nature* **486**, 101–104 (2012).

12. Rizo, H. *et al.* Preservation of Earth-forming events in the tungsten isotopic composition of modern flood basalts. *Science* **352**, 809–812 (2016).

13. Deschamps, F. & Tackley, P. J. Searching for models of thermo-chemical convection that explain probabilistic tomography. IIInfluence of physical and compositional parameters. *Physics of the Earth and Planetary Interiors* **176**, 1–18 (2009).

14. Li, M., McNamara, A. K. & Garnero, E. J. Chemical complexity of hotspots caused by cycling oceanic crust through mantle reservoirs. *Nature Geoscience* **7**, 366–370 (2014).

15. Nakagawa, T. & Tackley, P. J. Influence of combined primordial layering and recycled MORB on the coupled thermal evolution of Earth's mantle and core. *Geochemistry, Geophysics, Geosystems* **15**, 619–633 (2014).

16. Garnero, E. J. & McNamara, A. K. Structure and dynamics of Earth's lower mantle. *Science* **320**, 626–628 (2008).

17. Deschamps, F., Cobden, L. & Tackley, P. J. The primitive nature of large low shear-wave velocity provinces. *Earth and Planetary Science Letters* **349**, 198–208 (2012).

18. Busse, F. Multiple solutions for convection in a two component fluid. *Geophys. Res. Lett.* **9**, 519–522 (1982).

19. Hernlund, J. & Houser, C. On the distribution of seismic velocities in Earth's deep mantle. *Earth Planet. Sci. Lett.* **265**, 423–437 (2008).

20. Lekic, V., Cottaar, S., Dziewonski, A. & Romanowicz, B. Cluster analysis of global lower mantle tomography: A new class of structure and implications for chemical heterogeneity. *Earth Planet. Sci. Lett.* **357-358**, 68–77 (2012).

21. Fukao, Y., Widiyantoro, S. & Obayashi, M. Stagnant slabs in the upper and lower mantle transition region. *Rev. Geophys.* **39**, 291–323 (2001).

22. Fukao, Y. & Obayashi, M. Subducted slabs stagnant above, penetrating through, and trapped below the 660 km discontinuity. *J. Geophys. Res.* **118**, 5920–5938 (2013).

23. King, S., Frost, D. & Rubie, D. Why cold slabs stagnate in the transition zone. *Geology* **43**, 231–234 (2015).

24. Ballmer, M. D., Schmerr, N. C., Nakagawa, T. & Ritsema, J. Compositional mantle layering revealed by slab stagnation at ∼1000-km depth. *Science Advances* **1**, doi:10.1126/sciadv.1500815 (2015).

25. Cottaar, S. & Lekic, V. Morphology of seismically slow lower-mantle structures. *Geophysical Journal International* **207**, 1122–1136 (2016).

26. Grand, S. P. Mantle shear-wave tomography and the fate of subducted slabs. *Philosophical Transactions of the Royal Society of London A: Mathematical, Physical and Engineering Sciences* **360**, 2475–2491 (2002).

27. Jackson, I. Elasticity, composition, and temperature of the Earth's lower mantle: A reappraisal. *Geophys. J. Int.* **134**, 291–311 (1998).

28. Murakami, M., Ohishi, Y., Hirao, N. & Hirose, K. A perovskitic lower mantle inferred from high–pressure, high–temperature sound velocity data. *Nature* **485**, 90–95 (2012).

29. Valencia-Dardona, J., Shukla, G., Wu., Z., Yuen, D. & Wentzcovitch, R. Impact of spin crossover in ferropericlase on the lower mantle adiabat. *Geophys. Res. Lett.* in review (2016).

30. da Silva, C., Wentzcovitch, R., Patel, A., Price, G. & Karato, S. The composition and geotherm of the lower mantle: Constraints from the calculated elasticity of silicate perovskite. *Phys. Earth Planet. Int.* **118**, 103–109 (2000).

31. Karki, B., Wentzcovitch, R., de Gironcoli, S. & Baroni, S. First principles thermoelasticity of $MgSiO_3$-perovskite: Consequences for the inferred properties of the lower mantle. *Geophys. Res. Lett.* **28**, 2699–2702 (2001).

32. Wentzcovitch, R., Karki, B., Cococcioni, M. & de Gironcoli, S. Thermoelastic properties of of $MgSiO_3$-perovskite: Insights on the nature of the Earth s lower mantle. *Phys. Rev. Lett.* **92**, doi:10.1103/PhysRevLett.92.018501 (2004).

33. Wentzcovitch, R. *et al.* Anomalous compressibility of ferropericlase throughout the iron spin crossover. *Proc. Natl. Acad. Sc. USA* **106**, 8447–8452 (2009).

34. Xu, W., Lithgow-Bertelloni, C., Stixrude, L. & Ritsema, J. The effect of bulk composition and temperature on mantle seismic structure. *Earth Planet. Sci. Lett.* **275**, 70–79 (2008).

35. Wang, X., Tsuchiya, T. & Hase, A. Computational support for a pyrolitic lower mantle containing ferric iron. *Nature Geoscience* **8**, 556–560 (2015).

36. Wu, Z. Velocity structure and composition of the lower mantle with spin crossover in ferropericlase. *J. Geophys. Res.* **121**, 2304–2314 (2016).

37. Dziewonski, A. & Anderson, D. Preliminary reference Earth model. *Phys. Earth Planet. Inter.* **25**, 297–356 (1981).

38. Shukla, G. *et al.* Thermoelasticity of Fe^{2+}-bearing bridgmanite. *Geophys. Res. Lett.* **42**, 1741–1749 (2015).

39. Wu, Z., Justo, J., da Silva, C., de Gironcoli, S. & Wentzcovitch, R. M. Anomalous thermodynamic properties in ferropericlase throughout its spin crossover transition. *Physical Review B* **80**, doi:10.1103/PhysRevB.80.014409 (2009).

40. Wu, Z. & Wentzcovitch, R. Spin crossover in ferropericlase and velocity heterogeneities in the lower mantle. *Proc. Nat. Academy Sci.* **111**, 10468–10472 (2014).

41. Cobden, L. *et al.* Thermochemical interpretation of 1-D seismic data for the lower mantle: The significance of nonadiabatic thermal gradients and compositional heterogeneity. *Journal of Geophysical Research: Solid Earth* **114**.

42. Cottaar, S., Heister, T., Rose, I. & Unterborn, C. BurnMan: A lower mantle mineral physics toolkit. *Geochemistry, Geophysics, Geosystems* **15**, 1164–1179 (2014).

43. Matas, J., Bass, J., Ricard, Y., Mattern, E. & Bukowinski, M. On the bulk composition of the lower mantle: predictions and limitations from generalized inversion of radial seismic profiles. *Geophysical Journal International* **170**, 764–780 (2007).

44. Mattern, E., Matas, J., Ricard, Y. & Bass, J. Lower mantle composition and temperature from mineral physics and thermodynamic modelling. *Geophysical Journal International* **160**, 973–990 (2005).

45. Ricolleau, A. *et al.* Density profile of pyrolite under the lower mantle conditions. *Geophysical Research Letters* **36**, doi:10.1029/2008GL036759 (2009).

46. Khan, A., Connolly, J. & Taylor, S. Inversion of seismic and geodetic data for the major element chemistry and temperature of the Earth's mantle. *Journal of Geophysical Research: Solid Earth* **113**, doi:10.1029/2007JB005239 (2008).

47. Houser, C. & Williams, Q. The relative wavelengths of fast and slow velocity anomalies in the lower mantle: Contrary to the expectations of dynamics? *Phys. Earth Planet. Int.* **176**, 187–197 (2009).

48. Green, D., Hibberson, W. & Jaques, A. Petrogenesis of mid-ocean ridge basalts. In McElhinny, M. (ed.) *The Earth: Its Origin, Structure and Evolution*, 265–299 (Academic Press, 1979).

49. Brown, J. & Shankland, T. Thermodynamic parameters in the Earth as determined from seismic profiles. *Geophys. J. R. Astron. Soc.* **66**, 579–596 (1981).

7 Supplementary Movie Captions

Supplementary Movie S1: Animation of mantle compositional evolution over 15 Gyrs model time for the example case (see Suppl. Table S3 for parameters). Mantle-convection patterns are stable over at least 15 Gyrs due to the persistence of intrisically strong BEAMS. For snapshots of this animation and colorscale, see Figure 1c,f in the main text. Tickmarks are in (km).

Supplementary Movie S2: Animation of mantle potential temperature over 15 Gyrs model time for the example case (see Suppl. Table S3 for parameters). For a snapshot of this animation and colorscale, see Figure 1d in the main text. Tickmarks are in (km).

Supplementary Movie S3: Animation of mantle compositional evolution over 4.6 Gyrs model time for reference case I (see Suppl. Table S3 for parameters). Mantle-convection patterns are chaotic and yield efficient mixing. For a snapshot of this animation and colorscale, see Figure 1b in the main text. Tickmarks are in (km).

Supplementary Movie S4: Animation of mantle potential temperature over 4.6 Gyrs model time for the example case (see Suppl. Table S3 for parameters). For a snapshot of this animation and colorscale, see Figure 1a in the main text. Tickmarks are in (km).

8 Supplementary Figure Captions

Supplementary Figure S1: Model initial conditions for all cases with composition (colors) and temperatures (contours, spaced 450K).

Supplementary Figure S2: Seismic velocities and density calculated for a uniform pyrolite composition (blue) and an idealized BEAMS mantle (magenta). The idealized BEAMS mantle is composed of 50% bridgmanite (high-viscosity ambient mantle), and 25% each cold and warm harzburgite (downwellings and upwellings, respectively). Black dots show PREM values[37]. Both scenarios are practically indistinguishable; differences are smaller than seismic-model resolution.

Supplementary Figure S3: Calculated density as well as shear-, bulk-, and compressional velocities for bridgmanite (magenta), pyrolite (blue), and harzburgite (green) (for compositions, see Suppl. Table 1). The geotherms for each of these compositions are shown in Supplementary Figure S4. Also see method section.

Supplementary Figure S4: Geotherms for each of the compositions described in Suppl. Table 1. Geotherms are a self-consistent output from the ab-initio calculations (see method section). Dashed and dotted green lines show temperature profiles for warm and cold harzburgite, respectively, as have been used to calculate the average BEAMS mantle shown in Supplementary Figure S2. Likewise, the dashed magenta line is the temperature profile for the warm bridgmanite as shown in Supplementary Figure S8. Geotherms for warm/cold compositions are calculated from foot temperatures at the top of the lower mantle that are shifted by +/- 500 K. The brown line is the adiabatic geotherm from ref. [49] for reference.

Supplementary Figure S5: Schematic viscosity variations for a lower-mantle assemblage containing both a strong Br and weak Fp phase. The viscosities of either Br or Fp involve uncertainties, as do rheological models and lower-mantle composition. Here we juxtapose the expected viscosity of BEAMS-like material with solar-chondritic Mg/Si (orange bar) with that of pyrolitic material (blue bar) in the lower mantle. The rheology of lower-mantle materials is bracketed by the "load-bearing framework" (LBF) model and the non-linear "inter-connected weak layers" (IWL) model. That said, the IWL model (solid line) is more realistic than the LBF model (dashed line) for a two-phase mixture with large viscosity contrast[2,4], particularly in high-strain regions such as predicted by our models for pyrolitic up-/downwelling conduits. Schematic distributions of strong Br (white) and weak Fp (black) grains are shown as inset images. Note that in the IWL model the largest change in viscosity occurs as the fraction of weak phase (Fp) varies between 0% and about 30%.

Supplementary Figure S6: Histograms of composition after 4.6 Gyrs model time for cases with (A) variable Φ at the same $\Delta\rho$, and (B) variable $\Delta\rho$ at the same Φ. Note that all reference cases are also represented in (A) as dashed lines, including reference case I with $\Delta\rho = 0$ kg/m^3. In addition to a sharp peak at compositional index 0 (pure pyrolite/harzburgite composition in the shallow mantle according to model assumptions), cases either display a unimodal distribution of composition throughout the model domain (with one peak at compositional index $\sim$0.5; i.e. relatively well-mixed: regime A), or a bimodal distribution (with another peak at $>$0.84; i.e. preservation of SiO_2-rich material: remime B). The white histogram in front of the grey shading shows the original distribution of lower-mantle material at time-step zero (scaled by a factor of 0.25) for comparison. The red line is the same in both panels, and marks the example case visualized in Figure 1c-f. All other cases as labeled.

Supplementary Figure S7: Lateral seismic velocity variations of warm and cold harzburgite relative to ambient mantle of unknown composition. We vary the composition of the ambient adiabatic mantle, to which the warm (+500 K) or cold (-500 K) harzburgite is compared to, from pyrolitic to

bridgmanitic compositions. Addition of SiO_2 to the background ambient mantle lowers the seismic velocity contrast of cold downwelling material and amplifies the contrast of warm upwelling material. These conclusions hold even if the effects of basalt on seismic velocities in pyrolitic domains are included (not shown). For computation of thermoelastic properties, see method section.

Supplementary Figure S8: Calculated density as well as shear-, bulk-, and compressional velocities for warm (+500 K) bridgmanite. The geotherm associated with this calculation is the dashed magenta line in Supplementary Figure S4. For details, see method section.

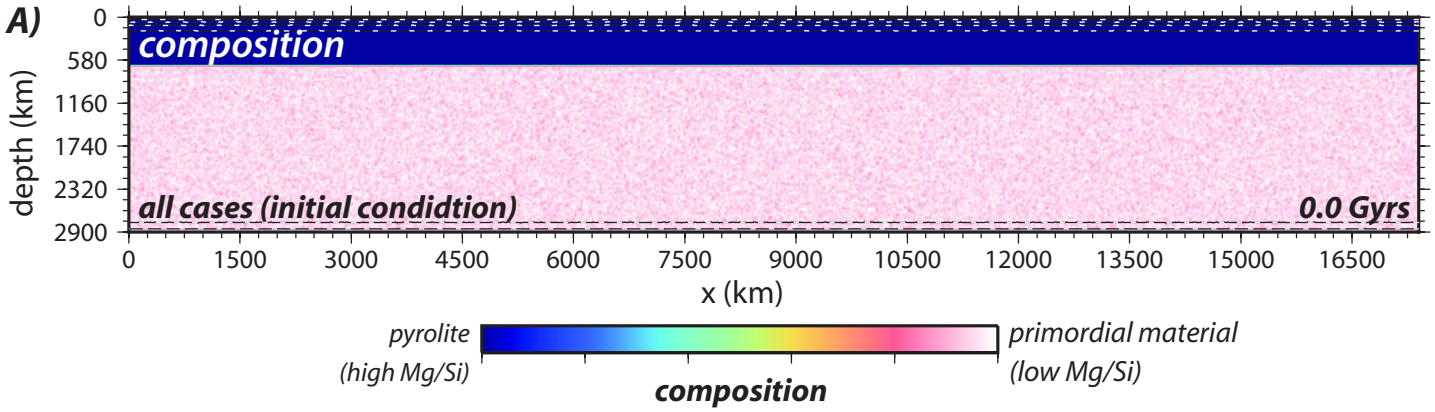

Supplementary Figure S1

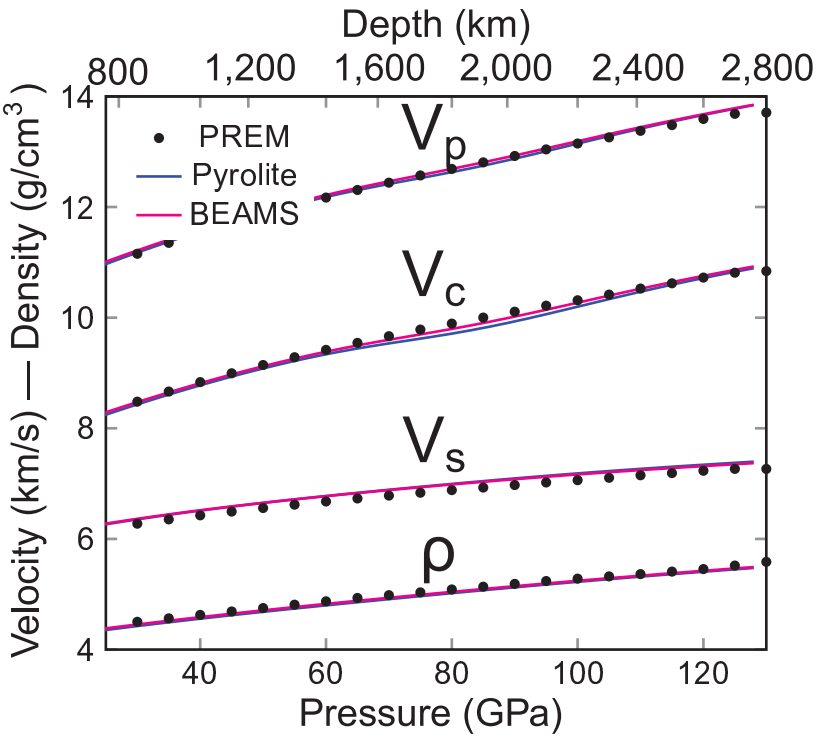

Supplementary Figure S2

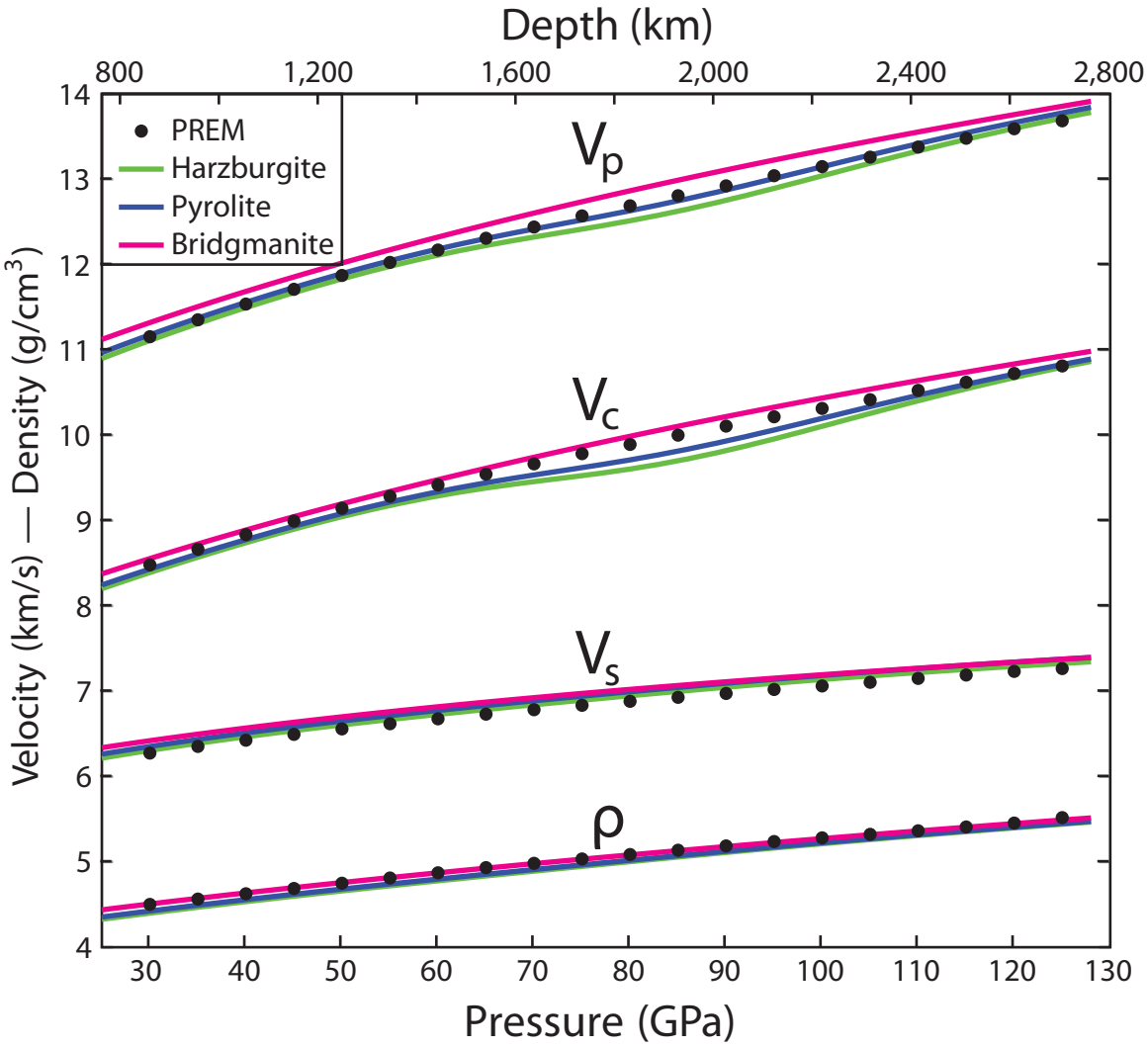

Supplementary Figure S3

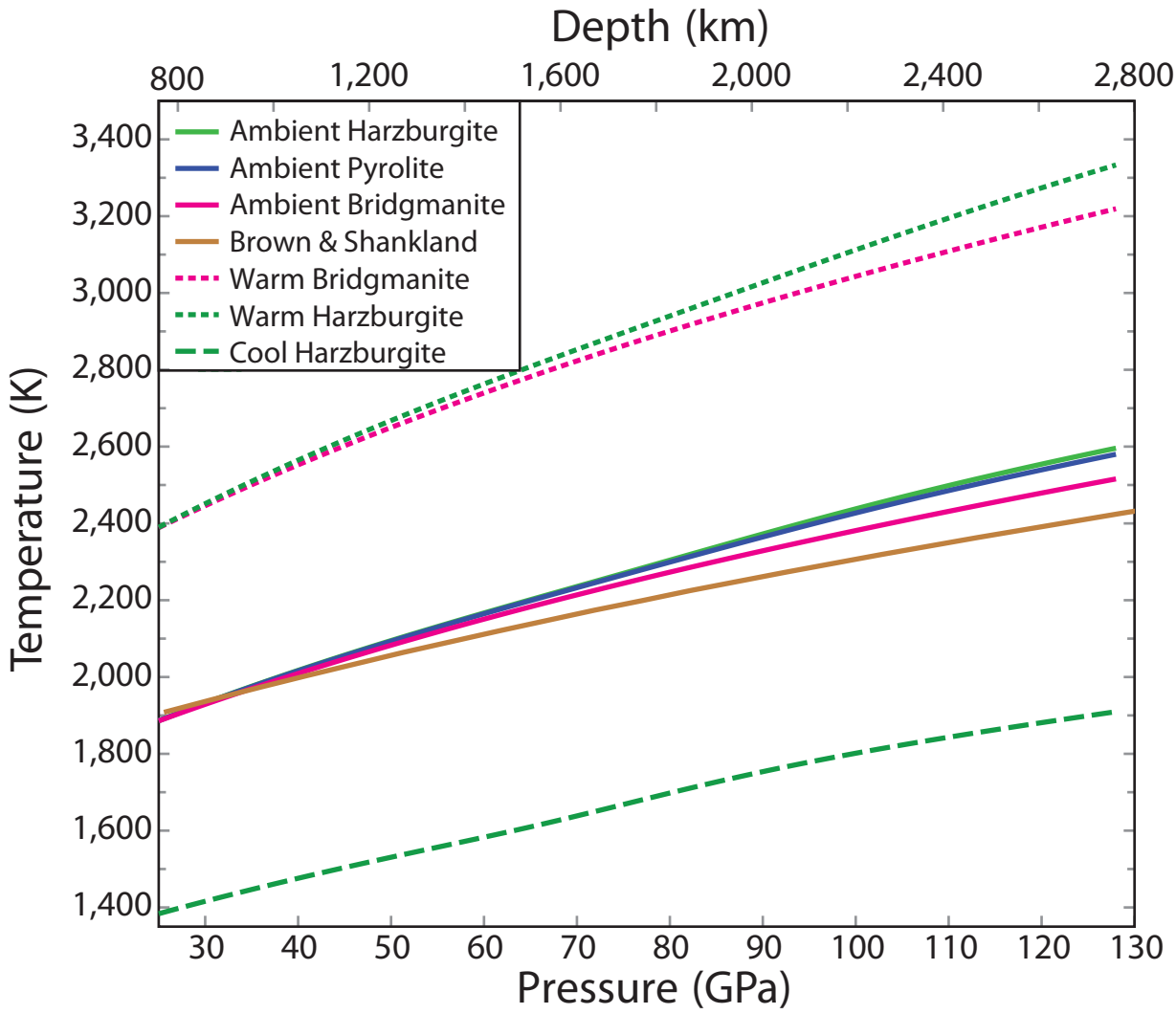

Supplementary Figure S4

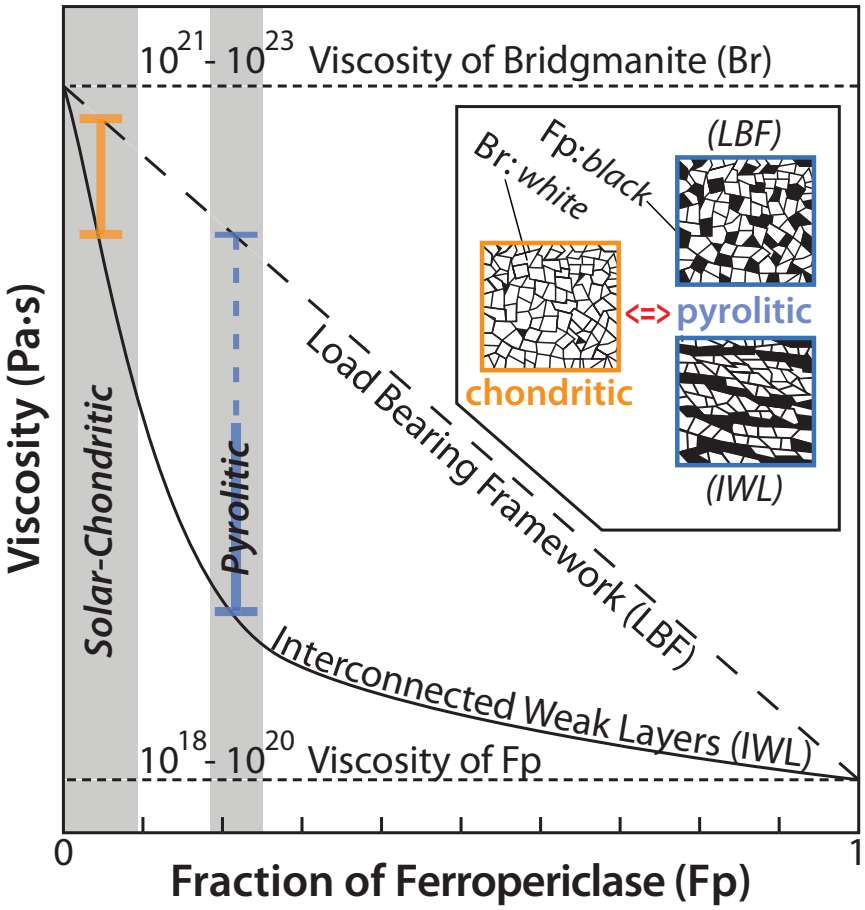

Supplementary Figure S5

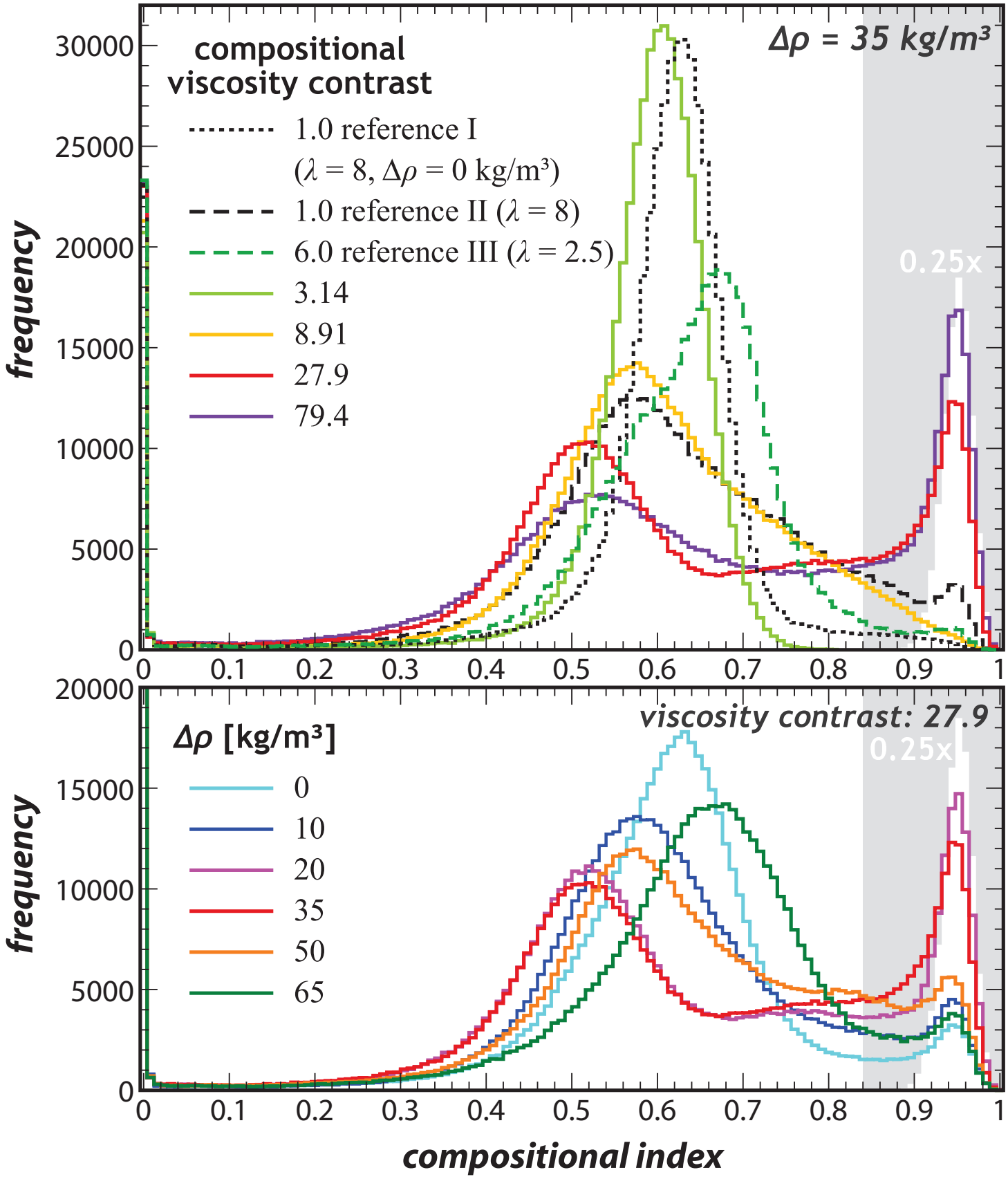

Supplementary Figure S6

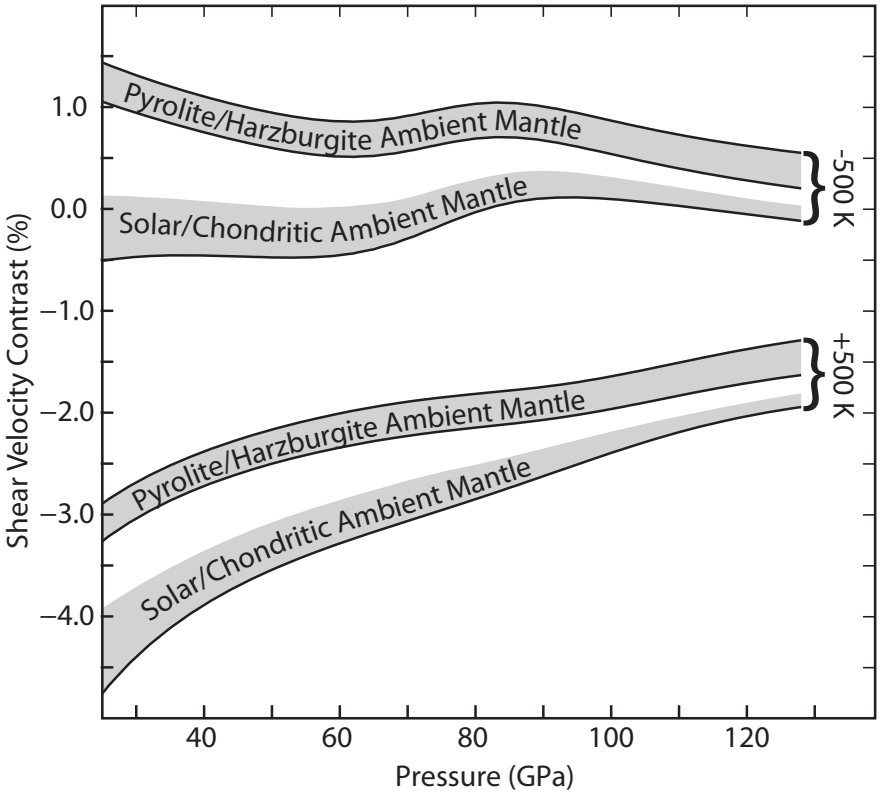

Supplementary Figure S7

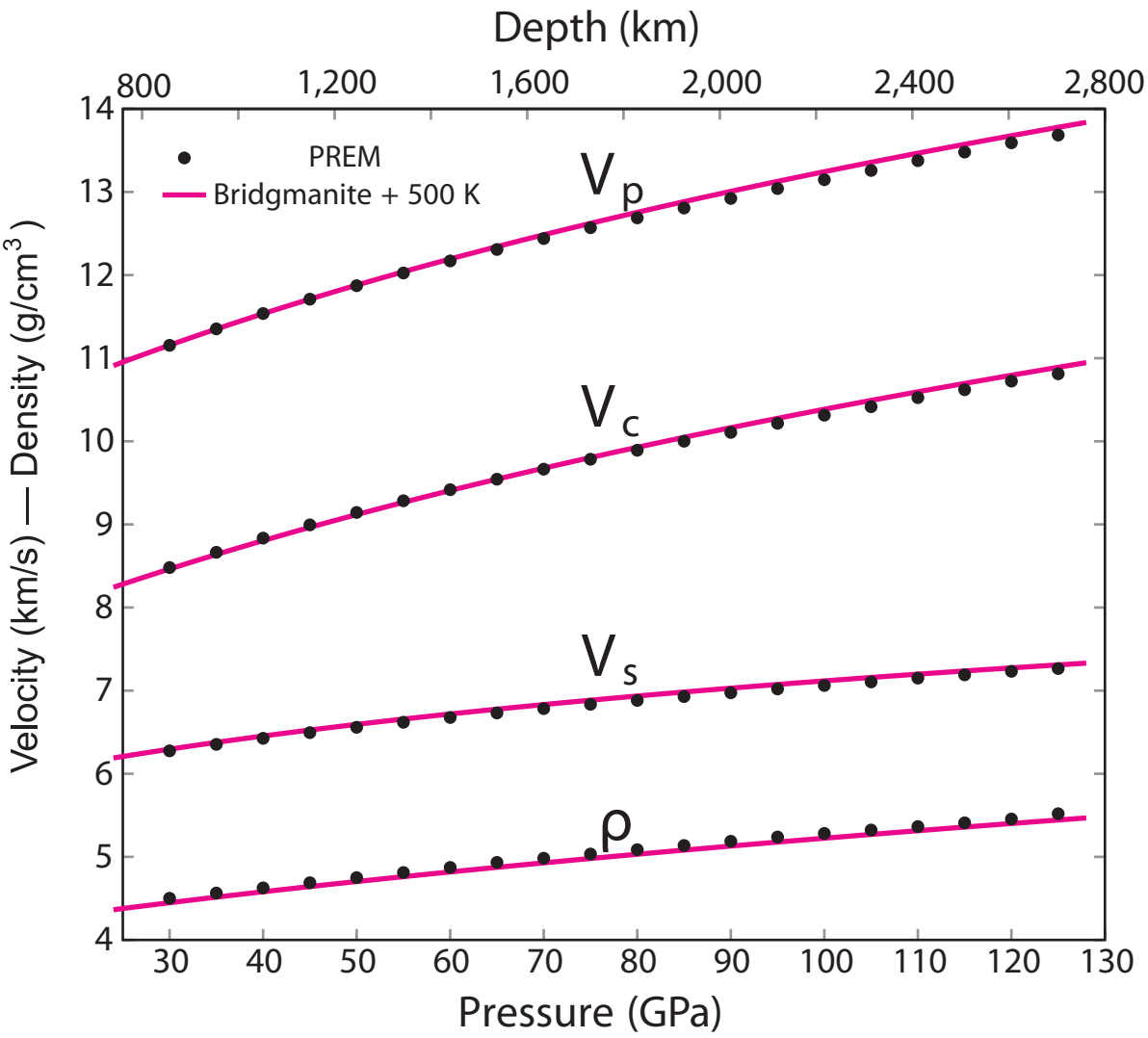

Supplementary Figure S8